

Northumbria Research Link

Citation: Karampelas, Konstantinos, McLaughlin, James, Botha, Gert and Regnier, Stephane (2022) Oscillatory Reconnection of a 2D X-point in a hot coronal plasma. The Astrophysical Journal, 925 (2). p. 195. ISSN 0004-637X

Published by: IOP Publishing

URL: <https://doi.org/10.3847/1538-4357/ac3b53> <<https://doi.org/10.3847/1538-4357/ac3b53>>

This version was downloaded from Northumbria Research Link:
<http://nrl.northumbria.ac.uk/id/eprint/47995/>

Northumbria University has developed Northumbria Research Link (NRL) to enable users to access the University's research output. Copyright © and moral rights for items on NRL are retained by the individual author(s) and/or other copyright owners. Single copies of full items can be reproduced, displayed or performed, and given to third parties in any format or medium for personal research or study, educational, or not-for-profit purposes without prior permission or charge, provided the authors, title and full bibliographic details are given, as well as a hyperlink and/or URL to the original metadata page. The content must not be changed in any way. Full items must not be sold commercially in any format or medium without formal permission of the copyright holder. The full policy is available online: <http://nrl.northumbria.ac.uk/policies.html>

This document may differ from the final, published version of the research and has been made available online in accordance with publisher policies. To read and/or cite from the published version of the research, please visit the publisher's website (a subscription may be required.)



Oscillatory Reconnection of a 2D X-point in a Hot Coronal Plasma

Konstantinos Karamelas^{1,2} , James A. McLaughlin¹ , Gert J. J. Botha¹ , and Stéphane Régnier¹ ¹Department of Mathematics, Physics and Electrical Engineering, Northumbria University, Newcastle upon Tyne, NE1 8ST, UK
konstantinos.karamelas@northumbria.ac.uk²Centre for mathematical Plasma Astrophysics, Department of Mathematics, KU Leuven, Celestijnenlaan 200B bus 2400, B-3001 Leuven, Belgium
Received 2021 September 17; revised 2021 November 12; accepted 2021 November 17; published 2022 February 4

Abstract

Oscillatory reconnection (a relaxation mechanism with periodic changes in connectivity) has been proposed as a potential physical mechanism underpinning several periodic phenomena in the solar atmosphere, including, but not limited to, quasi-periodic pulsations (QPPs). Despite its importance, however, the mechanism has never been studied within a hot, coronal plasma. We investigate oscillatory reconnection in a one million Kelvin plasma by solving the fully-compressive, resistive MHD equations for a 2D magnetic X-point under coronal conditions using the PLUTO code. We report on the resulting oscillatory reconnection including its periodicity and decay rate. We observe a more complicated oscillating profile for the current density compared to that found for a cold plasma, due to mode-conversion at the equipartition layer. We also consider, for the first time, the effect of adding anisotropic thermal conduction to the oscillatory reconnection mechanism, and we find this simplifies the spectrum of the oscillation profile and increases the decay rate. Crucially, the addition of thermal conduction does not prevent the oscillatory reconnection mechanism from manifesting. Finally, we reveal a relationship between the equilibrium magnetic field strength, decay rate, and period of oscillatory reconnection, which opens the tantalising possibility of utilizing oscillatory reconnection as a seismological tool.

Unified Astronomy Thesaurus concepts: [Magnetohydrodynamics \(1964\)](#); [Solar magnetic reconnection \(1504\)](#); [Solar coronal seismology \(1994\)](#); [Solar coronal waves \(1995\)](#); [Magnetohydrodynamical simulations \(1966\)](#)

1. Introduction

Null points are magnetic field singularities at which the magnetic field strength and Alfvén speed are zero. Although the coronal magnetic field is hard to measure directly (Lin et al. 2004; Gibson et al. 2016), potential field extrapolations from photospheric magnetograms predict that null points are omnipresent in the solar atmosphere (Galsgaard & Nordlund 1997; Brown & Priest 2001; Longcope 2005; Régnier et al. 2008). The presence of null points in the solar atmosphere drastically changes the behavior of waves and flows around them (e.g., Gruszecki et al. 2011; McLaughlin et al. 2011; Santamaria et al. 2015; Sabri et al. 2018, 2019). In McLaughlin & Hood (2004, 2005, 2006a, 2006b), the phenomenon of wave refraction around various 2D null points was established for both cold ($\beta = 0$) plasma and finite- β plasma. Those studies also found that, for finite- β plasma, a low- β fast wave can generate high- β fast and slow waves through mode conversion when crossing the equipartition layer, i.e., the layer where the Alfvén speed equals the sound speed. Thurgood & McLaughlin (2012, 2013) extended these results to 3D null points.

In addition, simulations involving 2D null points have shown the development of high-frequency wave trains (~ 80 MHz) in their vicinity (Santamaria et al. 2016, 2017), while in Santamaria & Van Doorsselaere (2018) it was shown that a null point behaves as a resonant cavity that can generate waves at specific frequencies depending on the background equilibrium (the latter is important in the context of coronal seismology; Uchida 1970; Roberts et al. 1984). Waves have also been generated via reconnection at 2D null points (e.g.,

Nishizuka et al. 2008; He et al. 2009) and compared directly with observations. The interaction of fast magnetoacoustic waves with a 2.5D null point has been shown to produce plasmoids due to the tearing mode instability in a numerical study (Sabri et al. 2020). Numerical simulations have shown that 3D null points act as sources of Alfvén waves (e.g., Lynch et al. 2014; Cranmer 2018), coronal jets in the form of propagating nonlinear Alfvén waves (Karpen et al. 2017), as well as other sources of fast and slow (and Alfvén) waves (Thurgood et al. 2017), when these 3D null points are subjected to various wave-based driving motions.

Apart from their interaction with the ubiquitous waves in the solar atmosphere (e.g., Nakariakov & Verwichte 2005; De Pontieu et al. 2007; Okamoto et al. 2007; Tomczyk et al. 2007; McIntosh et al. 2011), null points also play a key role in highly energetic phenomena such as solar flares (e.g., Shibata & Magara 2011). One way to achieve this is by dissipating the currents that are being accumulated at the null point, which leads to plasma heating, anomalous resistivity (via micro-instabilities), and, ultimately, reconnection (Nakariakov et al. 2006).

Reconnection occurs when strong currents allow neighboring magnetic field lines to diffuse, leading to a change in connectivity (e.g., Parker 1957; Sweet 1958; Petschek 1964) and is expected to occur at null points (Priest & Forbes 2000). While considering the relaxation of a 2D X-point that had been disturbed from equilibrium, Craig & McClymont (1991) identified oscillatory reconnection as a means of dissipating magnetic energy. As the name suggests, oscillatory reconnection describes a series of reconnection events associated with periodic changes in the connectivity of the magnetic field. A key characteristic of oscillatory reconnection is that its periodicity is not determined by a periodic external force, rather the periodicity manifests from a relaxation mechanism



Original content from this work may be used under the terms of the [Creative Commons Attribution 4.0 licence](#). Any further distribution of this work must maintain attribution to the author(s) and the title of the work, journal citation and DOI.

following from a finite, aperiodic initial perturbation (similar to a decaying harmonic oscillation).

Oscillatory reconnection was further studied in a 2D X-point for finite- β and nonlinear effects in McLaughlin et al. (2009). In that study, an initially cold ($\beta=0$) plasma setup was considered, but the solution included the full compressible resistive MHD equations and thus allowed for plasma heating to take place. This mechanism has also been studied for a 3D null point in Thurgood et al. (2017), where the by-product of oscillatory reconnection was the generation of freely propagating MHD waves, escaping the vicinity of the null point. Additional studies have focused on the periodicity of oscillatory reconnection from linear and nonlinear perturbations, and how it is affected by resistivity and the amplitude of the initial perturbation (McLaughlin et al. 2012a; Thurgood et al. 2018a, 2018b, 2019).

As a mechanism, oscillatory reconnection is an appealing explanation of quasi-periodic pulsations (QPPs), which have now been detected in a multitude of solar flares (e.g., Kupriyanova et al. 2016; Van Doorsselaere et al. 2016; Pugh et al. 2017; Yuan et al. 2019; Hayes et al. 2020; Li et al. 2020a, 2020b, 2021; Clarke et al. 2021) as well as in a variety of stellar flares (e.g., Broomhall et al. 2019; Guarcello et al. 2019; Jackman et al. 2019; Notsu et al. 2019; Vida et al. 2019; Mancuso et al. 2020; Ramsay et al. 2021). QPPs are now understood to be a central feature of the flaring process, and thus understanding the true underpinning mechanism for QPPs holds the key to understanding solar and stellar flares. Detailed reviews of the possible mechanism(s) underpinning QPPs can be found in McLaughlin et al. (2018), Kupriyanova et al. (2020), and Zimovets et al. (2021).

Oscillatory reconnection is also a possible mechanism behind phenomena like periodicities observed in jets (Hong et al. 2019), periodic behavior associated with the formation, disappearance, and eruption of magnetic flux ropes (Shen et al. 2018; Xue et al. 2019), and quasi-periodic flows associated with spicules in the solar atmosphere (e.g., De Pontieu & McIntosh 2010; De Pontieu et al. 2011; Samanta et al. 2019; Yurchyshyn et al. 2020). For spicules, a 2D flux emergence model that triggered the oscillatory reconnection mechanism was able to reproduce such flows with the observed periodicities (McLaughlin et al. 2012b). Oscillatory reconnection may also be a possible explanation of phenomena now being observed by the Parker Solar Probe (e.g., Bale et al. 2016, 2019; Kasper et al. 2019) including Alfvénic spikes/kinks (He et al. 2021) and periodicities correlated with Type III radio bursts (Cattell et al. 2021).

Even though oscillatory reconnection has been used within the context of a realistic stratified solar atmosphere (Murray et al. 2009; McLaughlin et al. 2012b), so far there has been no thorough study of the mechanism in hot, coronal plasma. In this paper, we will take that next step by investigating the oscillatory reconnection mechanism within a hot plasma under coronal conditions. After describing the details of the numerical setups used in our studies (Section 2), we will present our results on the initiation and evolution of oscillatory reconnection for hot plasma (Section 3.1) while providing a direct comparison to the cold plasma case. We will address the effects of anisotropic thermal conduction (Section 3.2), which is a necessary step toward a more realistic coronal environment, and we will present the results of our parameter study regarding the magnetic field strength and its effects on the periodicity and

decay rate of oscillatory reconnection (Section 3.3). The conclusions are presented in Section 4, and the Appendix reports on a parameter study investigating the temperature dependence.

2. Numerical Setup

2.1. Numerical Scheme

Our setup closely follows that of McLaughlin et al. (2009). We solve the 2D compressible resistive MHD equations, also in the presence of numerical resistivity, using the PLUTO code (Mignone et al. 2007, 2012), a finite-volume, shock-capturing code, which uses double precision arithmetic for the computations. We employ the third-order Runge–Kutta method to calculate the time step, the fifth-order monotonicity preserving scheme (MP5) for the spatial integration, and the total variation diminishing Lax–Friedrich (TVDLF) solver. To keep the solenoidal constraint on the magnetic field, we employ the Constrained Transport method.

The 2D compressible and resistive MHD equations, in the absence of gravity, written for the primitive variables are:

$$\frac{\partial \rho}{\partial t} + \nabla \cdot (\rho \mathbf{v}) = 0, \quad (1)$$

$$\rho \left[\frac{\partial \mathbf{v}}{\partial t} + \rho (\mathbf{v} \cdot \nabla) \mathbf{v} \right] = -\nabla p + \frac{1}{\mu} (\nabla \times \mathbf{B}) \times \mathbf{B}, \quad (2)$$

$$\rho \left[\frac{\partial \epsilon}{\partial t} + (\mathbf{v} \cdot \nabla) \epsilon \right] = -p \nabla \cdot \mathbf{v} + \frac{1}{\sigma} |\mathbf{J}|^2 + \Lambda, \quad (3)$$

$$\frac{\partial \mathbf{B}}{\partial t} = \nabla \times (\mathbf{v} \times \mathbf{B}) + \eta \nabla^2 \mathbf{B}, \quad (4)$$

where the quantities ρ , p , and \mathbf{v} are the density, plasma pressure, and velocity, respectively. The magnetic field \mathbf{B} satisfies the condition $\nabla \cdot \mathbf{B} = 0$, and the electric current is defined as $\mathbf{J} = \nabla \times \mathbf{B} / \mu$. In addition, $\mu = 4\pi \times 10^{-7} \text{ H m}^{-1}$ is the magnetic permeability, σ is the electrical conductivity, $\eta = 1/\mu\sigma$ is the magnetic diffusivity, and $\epsilon = p/[\rho(\gamma - 1)]$ is the specific internal energy density. Finally, $\gamma = 5/3$ is the ratio of the specific heats, and Λ represents the volumetric energy gain/loss terms, such as anisotropic thermal conduction.

We use Cartesian coordinates (x, y) and express all quantities in code units. A code variable U_c is converted to its physical units U with the help of the normalization unit U_0 , i.e., $U = U_0 U_c$. The constants U_0 are specified such that the values of the quantities match the conditions in the solar corona. Specifically, $x_0 = y_0 = L_0 = 10^6 \text{ m}$ is the unit length, $\rho_0 = 10^{-12} \text{ kg m}^{-3}$ the unit density, $v_0 \sim 129 \times 10^3 \text{ m s}^{-1}$ the unit velocity (equal to $c_s/\sqrt{\gamma}$, where c_s the sound speed of coronal plasma at 1 MK), $p_0 = \rho_0 v_0^2$ the unit pressure, $T_0 = 10^6 \text{ K}$ the unit temperature, $B_0 = \sqrt{\mu p_0} = 1.44 \text{ G}$ the unit magnetic field, and $t_0 = L_0/v_0 = 7.78 \text{ s}$ the unit time. We also let $\nabla = \nabla_c/L_0$. Finally, the magnetic diffusivity takes values $\eta = \eta_0 \eta_c = v_0 L_0 R_m^{-1}$, where R_m is the magnetic Reynolds number, assuming that v_0 and L_0 are the typical velocity and length scales of the system, respectively. In this setup, we take $R_m = 10^5$ and thus $\eta_c = 10^{-5}$. Alongside the explicit magnetic diffusivity, we also have inevitable effects of the ‘effective’ numerical diffusivity present in our code. Through a parameter study, we have estimated the effective numerical diffusion of our lower-resolution setups used in this study to be between 10^{-6} and 10^{-5} in code units. The effective numerical diffusion of the

higher resolution setups is thus lower than this value, since it decreases with an increasing resolution. This numerical dissipation is many orders of magnitude higher than the values for the diffusivity expected in the solar corona, which is why we chose such a relatively small value for R_m . We also need to stress that the small value for R_m makes it difficult to make accurate quantitative estimations for the solar corona, but it will still allow us to get qualitative results for the topic under study.

When switching on anisotropic thermal conduction (TC) in the PLUTO code, we use values of the parallel and perpendicular coefficients that are derived from the Spitzer conductivity (Orlando et al. 2008). The values for the parallel and perpendicular coefficients (in $\text{J s}^{-1} \text{K}^{-1} \text{m}^{-1}$) are the following:

$$\kappa_{\parallel} = 5.6 \times 10^{-12} T^{\frac{5}{2}}, \quad (5)$$

$$\kappa_{\perp} = 3.3 \times 10^{-21} T^{\frac{3}{2}} \frac{n_H^2}{\sqrt{TB^2}}, \quad (6)$$

where n_H is the hydrogen number density, and T and B are in physical units.

Finally, we note that for the rest of the paper, we will write the quantities for the code variables as U instead of U_c and show them in code units, unless otherwise stated.

2.2. Initial and Boundary Conditions

Just like in McLaughlin et al. (2009), our setup consists of a square domain containing a 2D magnetic X-point. Our domain consists of a structured uniform grid that extends to $(x, y) \in (-10, 10)$ code units, with a resolution of 2401×2401 grid points (and 1801×1801 grid points for the parameter studies in Section 3 and in the Appendix).

We consider a uniform density equal to $\rho_0 = 10^{-12} \text{ kg m}^{-3}$ and a temperature that is equal to $T_0 = 1 \text{ MK}$ (with the exception of the parameter study; see the Appendix). We take the equilibrium density to be uniform, as a spatial variation in density can cause phase mixing (e.g., Heyvaerts & Priest 1983). This creates a uniform initial sound speed V_S .

The initial magnetic field is given by:

$$\mathbf{B} = \frac{B_0}{L_0}(y, x, 0), \quad (7)$$

where B_0 is the characteristic field strength (taken equal to the unit magnetic field), and L_0 is the length scale for magnetic field variations (taken here as the unit length). This magnetic field takes its highest values at the boundaries and goes to zero at the X-point. The Alfvén speed V_A increases the farther we go away from the X-point (the origin in our simulations). The contour where $V_A = V_S$ defines the equipartition layer, and this is initially a circle (it will deform as the system evolves). In most parts of the solar corona, plasma- β is much less than unity but near null points plasma- β becomes large (since the magnetic field strength is itself becoming small). Thus, the equipartition layer defines a system where outside is a low- β environment and inside is a high- β environment.³

³ Note that the key parameter here is the location of the equipartition layer as opposed to the $\beta = 1$ layer, since the coupling between fast and slow waves is most efficient where $V_A = V_S$. For interest, the radius of the $\beta = 1$ layer occurs at a slightly greater radius (specifically a radius $\sqrt{\frac{2}{7}} \approx 1.095$ greater than the equipartition radius).

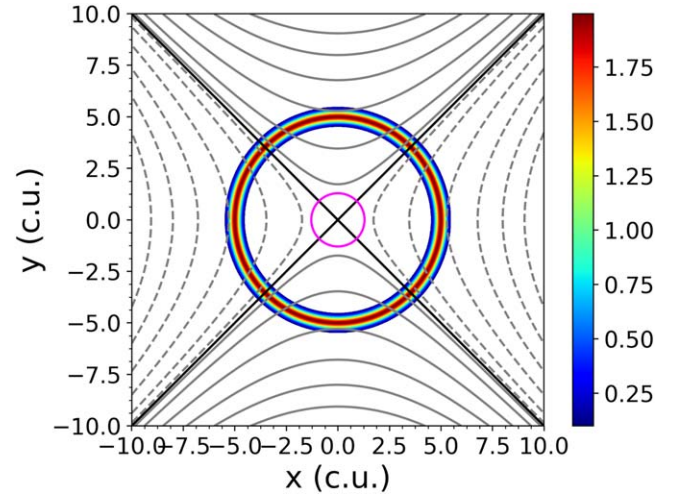


Figure 1. Initial conditions for the X-point setup. The magnetic field is shown with gray solid and dashed lines to highlight the different regions as separated by the separatrices (solid black lines). The initial v_{\perp} is shown here, cropped at its lower values for easier visualisation. The equipartition layer (magenta line) where $V_A = V_S$ is also shown here.

Following McLaughlin et al. (2009), in this paper, we consider an initial condition in velocity, such that:

$$v_{\perp} = \frac{C}{0.2\sqrt{2\pi}} \exp\left[-0.5\frac{(r-5)^2}{0.2}\right], \quad (8)$$

$$v_{\parallel}(t=0) = 0, \quad (9)$$

where $v_{\perp} = (\mathbf{v} \times \mathbf{B}) \cdot \hat{\mathbf{z}}$ is related to the velocity perpendicular to the magnetic field lines, and $v_{\parallel} = \mathbf{v} \cdot \mathbf{B}$ is related to the velocity parallel to the magnetic field lines. We will consider $C = 1$, unless otherwise stated, which brings us to the nonlinear regime of the wave-null point interaction, as in McLaughlin et al. (2009). The magnetic field configuration and the initial pulse are shown in Figure 1. The initial conditions for the velocity describe a circular velocity pulse in v_{\perp} , which crosses the magnetic field lines as it propagates, and can thus be identified as an (initially) fast magnetoacoustic wave. At the start of the simulation, the initial velocity pulse splits into two counterpropagating waves, each with half the velocity amplitude of the initial pulse. As shown in Figure 2, the first wave is traveling toward the null point and is the one we will be focusing on for the rest of this study, while the second wave is traveling away from the null point and toward the edges of our domain.

We take what are effectively reflective boundaries for the velocity across the boundaries, by fixing the velocity components to zero there, and use constant gradient boundary conditions for the magnetic field (of the form $d_i - d_{i-1} = d_{i-1} - d_{i-2}$). This ensures that, for a Cartesian grid, no currents are developed artificially at the boundaries. Finally, we fix the values of the pressure and density at the boundaries to their initial conditions. This allows for heat to freely leave the domain and not accumulate at the boundaries in the case where thermal conduction is used.

2.3. Additional Numerical Considerations: Damping Regions and the Solenoidal Constraint

Our numerical domain covers $(x, y) \in (-10, 10)$ code units, but our primary interest is in a much smaller region around the

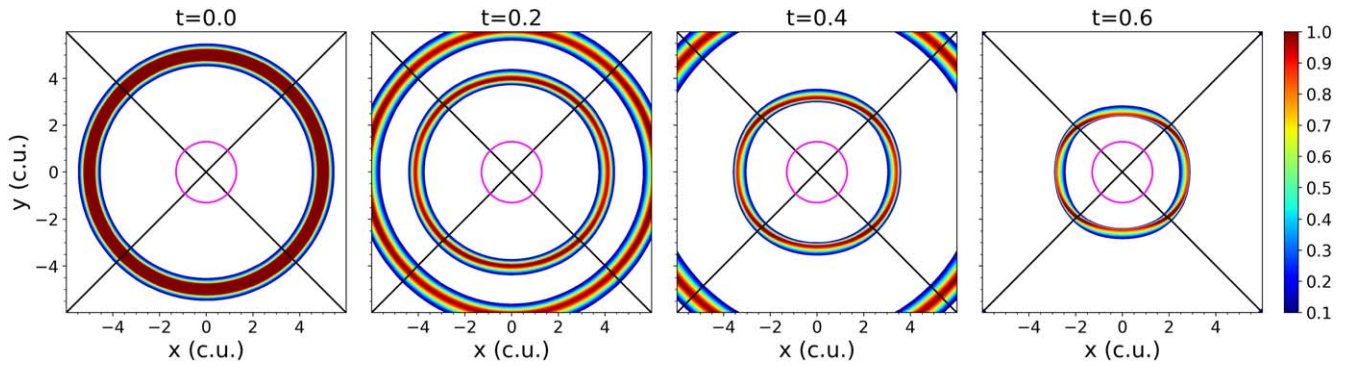


Figure 2. Zoomed in profiles of the v_x for the initial states of the simulation. The split of the initial pulse in an inward and outward traveling pulse is shown. The magnetic field separatrixes (black solid lines) and the equipartition layer (magenta solid line) are included.

null point itself. We employ a few different numerical strategies to ensure that our reflective boundaries will not result in reflected/returning waves contaminating the solution near the X-point. First, in order to deal with the outgoing pulse generated by our initial conditions, we reset the velocity after a radius of $r \geq 7$ at $t = 0.6$ (both in code units), removing the initial outward propagating velocity pulse.

Once this initial perturbation is removed, we initiate a numerical dissipation scheme for the velocity, for a radius of $r \geq 6$ and time $t > 0.6$ of the form $v_i = v_i/n_d$. This creates a damping region that removes kinetic energy from the outgoing waves and their reflections from the boundaries, per iteration, before they can reach the X-point and interfere with the solution. The dissipation coefficient $n_d = 1 + 0.007 \tanh(r - 6)^2$ regulates how fast the weakening will occur.

In addition to the numerical dissipation scheme, we introduce viscosity into our system, with coefficient $n_{visc} = 0.5 \tanh(r - 6)^2$, again in code units, for a radius of $r \geq 6$ and time $t > 0.6$. Both the viscous layer and the numerical damping scheme reduce the contamination of the area of interest from reflected waves.

Finally, we need to point out the importance of keeping the solenoidal constraint. The area of interest in our setups is in the vicinity of the X-point. There, by definition, the magnetic field goes to zero. Because of that, the numerical solution can be very sensitive to any type of errors associated with a poor treatment of the emerging $\nabla \cdot \mathbf{B} \neq 0$ numerical errors. To that end, we chose to use the Constrained Transport method, which is the most effective treatment provided with the PLUTO code to ensure the solenoidal constraint is satisfied.

3. Results

3.1. Oscillatory Reconnection in a 1 MK Coronal Plasma

Our first goal in this study is to explore oscillatory reconnection in the case of a hot coronal plasma; we will first focus on the setup with a resolution of 2401^2 grid points for an initial hot plasma of 1 MK in the absence of thermal conduction.

As was already mentioned, the initial velocity pulse described by Equations (8) and (9) splits into two counter-propagating waves, each with a velocity amplitude of $0.5 C$ (see Figure 2). The first wave travels toward the null point and is the one we focus on in this study. The other travels away from the null point and toward the boundaries of our computational domain, where it is removed by resetting the velocity components, as described in Section 2.3. Due to

refraction, the incoming pulse gradually focuses at the X-point and, because of the decreasing Alfvén speed profile, the length scales between the leading and trailing edges of the wave pulse contract (e.g., McLaughlin & Hood 2004, 2006b; McLaughlin et al. 2011). In agreement with the findings of McLaughlin et al. (2009), the incoming wave develops an asymmetry, with the wave peak at the trailing edge catching up with the leading footpoint of the pulse in the y -direction, while in the x -direction the footpoint of the pulse is catching up with the leading wave peak. This asymmetry was studied in terms of rarefaction and compression pulses in Gruszecki et al. (2011), where it was found that only smooth, low-amplitude pulses can reach a null point without overturning.

Once the incoming wave reaches the vicinity of the null point, it perturbs it from its initial (X-point) equilibrium. Following this initial perturbation, the system starts the process of oscillatory reconnection, where the initial collapse leads to reconnection, with the resulting restoring force causing an overshoot beyond its equilibrium state. As in McLaughlin et al. (2009), the system exhibits a series of reconnection events, with a periodically alternating connectivity. This periodicity can be traced by the formation of vertical/horizontal current sheets or their equivalent positive/negative values of the J_z current density at the null point, as can be seen in Figure 3. Also visible in the same figure is the accumulation of current density along what is essentially the location of the magnetic field separatrixes.

As shown in the top left panel of Figure 4, the profile of the J_z current density at the null point, following the initial perturbation, clearly exhibits an oscillatory behavior, with an amplitude which decays over time. This is in agreement with the results of McLaughlin et al. (2009) for 2D oscillatory reconnection in a cold plasma. This oscillatory behavior, which is a signature of oscillatory reconnection, persists over multiple periods, and can be roughly divided into two regimes: a regime where the amplitude decays over time, and a later regime, at $t \gtrsim 40$, where the profile fluctuates around a near-zero but positive asymptotic value for the J_z current density, equal to $J_z = 0.19$. The existence of an asymptotic nonzero value for the current density has been previously addressed for cold plasma and is associated with the (slightly) increased thermal pressure force on the left and right from the null point compared to above and below, due to an asymmetry in the produced heating. For a hot plasma, this asymmetry in the heating around the null point can be seen in Figure 5. In the left panel of this figure, we can see that plasma temperature increase is not symmetrical around the null point, but is oriented closer along

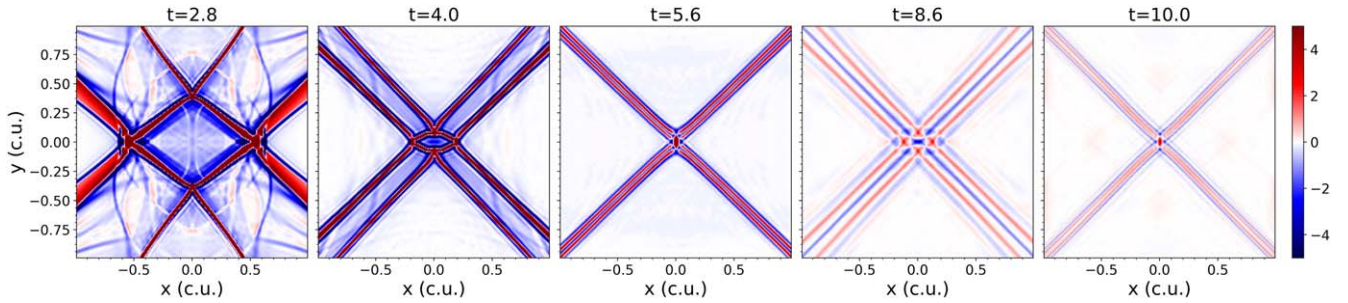


Figure 3. Zoomed in profile of the J_z current density. Shown here are the horizontal and vertical profiles associated with negative and positive values for the current density at the initial stages of the simulation.

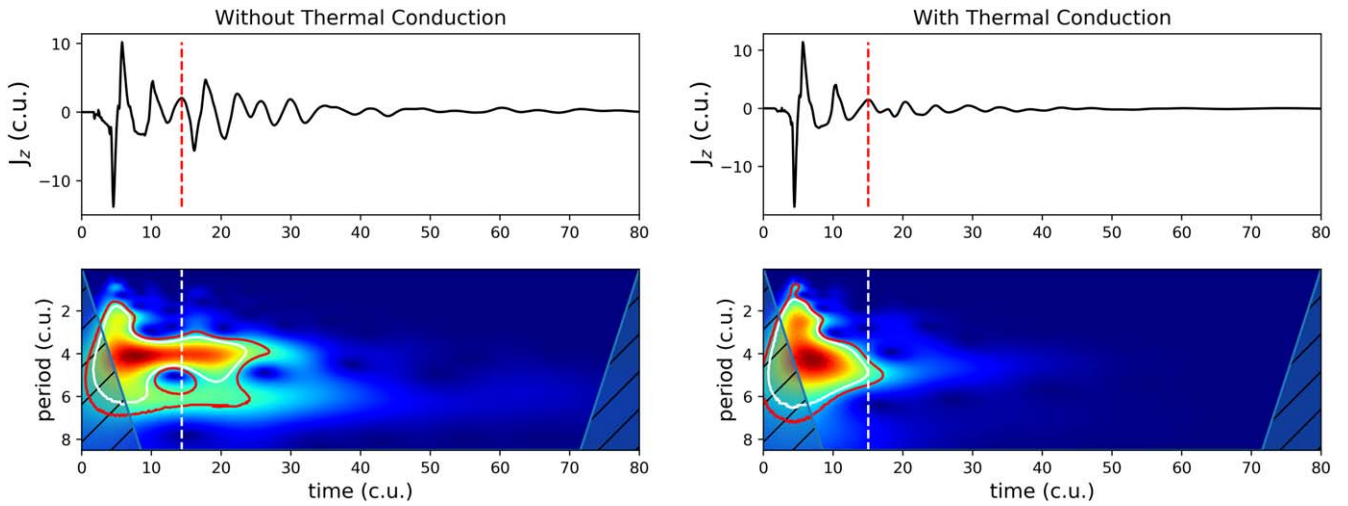


Figure 4. Top row: oscillating profile of the J_z current density at the X-point as a function of time. Bottom row: wavelet profile for the oscillating J_z current density. The vertical axis shows the oscillation period and the horizontal axis shows the time. The left panels show the results for the base setup with 1 MK, and the right show the results with anisotropic thermal conduction. The dashed lines show the time at which we estimate the oscillation period, while the solid red and white contours delineate the areas with confidence levels $\geq 80\%$ and $\geq 90\%$, respectively. The default magnetic field, as described in Equation (7), is equal to $B_0 = 1.44$ G.

the horizontal (x -axis). Note that there is nothing significant about the horizontal direction compared to the vertical; the orientation of the final asymmetry is dictated by the choice of incoming pulse asymmetry described previously.

The $J_z(0, 0, t)$ profile seen in the top left panel of Figure 4 shows a more complex behavior than that of a cold plasma. In particular, we see that the current density peak amplitudes fluctuate significantly, which hints toward the existence of additional waves perturbing the null point after the initial pulse perturbation. After performing a parameter study for setups of different base temperatures (see the Appendix for details), we attribute these additional waves to the effects of mode conversion at the equipartition layer.

Between the initial pulse location (radius $r = 5$) and the null point lies the equipartition layer, which is the layer where the Alfvén V_A speed equals the sound speed V_S . In our setup, due to the initial uniform plasma density and temperature, the sound speed is uniform everywhere, while the Alfvén speed increases further away from the null point. Thus the temperature of the setup and the strength of the magnetic field will affect the location of the equipartition layer. As the v_\perp pulse approaches this layer, shown with the magenta line in the panels of Figure 6, it starts to generate a velocity signal longitudinal to the magnetic field (v_\parallel). In McLaughlin & Hood (2004, 2005, 2006a, 2006b) and in Thurgood & McLaughlin (2012), the behavior of fast and slow MHD waves was

investigated in the neighborhood of various 2D and 3D null points. It was found that, for finite plasma- β , a low- β fast wave can generate high- β fast and slow waves through mode conversion when crossing the equipartition layer. Here, the velocity component perpendicular to the magnetic field corresponds to the (two) fast wave(s), while the component parallel to the field roughly corresponds to that generated slow MHD wave. As we see, there is extensive mode conversion happening not only along the equipartition layer but also inside the area defined by the layer. Given that, for hot plasma, in the context of our setup, this layer will include a larger area, we expect the mode conversion to generate the additional waves that perturb the J_z profile after the initiation of oscillatory reconnection.

Coming back to the top left panel of Figure 4, we have performed a wavelet analysis of the oscillation profile in order to identify its periodicity. This wavelet profile can be found on the bottom left panel of Figure 4. Once the initial perturbation takes place and the oscillation is set up, we can visually identify two different period bands, persisting for the larger part of the oscillation, and we calculate the respective periods. The first period is $4t_0 = 31.1$ s and is present up to approximately $35t_0$ with a confidence level $\geq 90\%$, while the second period is $6.2t_0 = 48.2$ s, with a confidence level $\geq 80\%$. Although the second period has a lower confidence level than the first, we believe that it is an important feature of the simulation, due

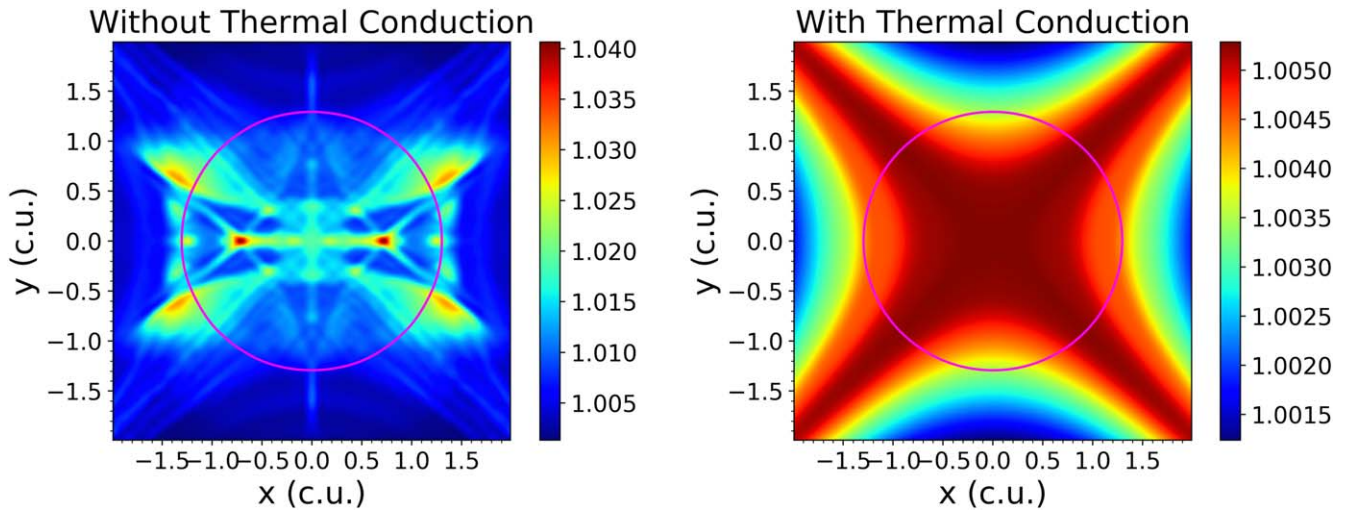


Figure 5. Left panel: temperature profile near the X-point for the setup with a base temperature of 1 MK, without thermal conduction. Right panel: the same temperature profile but for a simulation with anisotropic thermal conduction included. The equipartition layer (magenta line) is overplotted in both panels. The profiles are showing snapshots at $t = 80$, in code units. All the quantities are in code units.

to its persistence for the entirety of the simulation, even if its power and confidence level drop, especially after approximately $40t_0$. The values for the periods were calculated by using a Python script to find the maximum values along the dashed lines, located at the third positive J_z peak, as shown in Figure 4. We choose the value at the third peak to be consistent with the measurements in the following subsections, where this choice is further explained. Here we need to point out that, since we expect the oscillation periods to be dependent to an extent on the intensity of the reconnection procedure, these estimated values for the periods will be affected by the small values for the magnetic Reynolds number.

The presence of two periodic signals is something new that was not present in the previously studied system of oscillatory reconnection in a cold plasma. It is likely that this can be attributed to the extensive mode conversion taking place within the larger equipartition layer. The latter periodic signal ($6.2t_0 = 48.2$ s) can be attributed to the oscillatory reconnection process, due to its persistence for the entirety of the simulation, while the former periodic signal ($4t_0 = 31.1$ s) can be attributed to additional wave motions in the system, where those waves are generated by mode conversion as the fast wave initial condition crosses the equipartition layer (see also the Appendix for a direct comparison of the oscillating profiles for J_z for setups at different temperatures). It is the presence of these two signals that leads to a superimposed signal.

3.2. The Effect of Adding Thermal Conduction to the System

Our next step is to add anisotropic thermal conduction in the setup from Section 3.1. At coronal conditions for the temperature, the density and the magnetic field, the ratio of the parallel to perpendicular conduction coefficients (Equations (5) and (6)) is $\kappa_{\parallel} \gg \kappa_{\perp}$. That means that anisotropic thermal conduction is expected to dissipate heat predominantly along the magnetic field.

In the right panel of Figure 4, we see the $J_z(0, 0, t)$ profile and the corresponding wavelet profile for the setup with the anisotropic thermal conduction. From the profile for the current density, we see that oscillatory reconnection manifests as expected, and it exhibits a similar qualitative behavior as in the

case without thermal conduction. However, the two profiles show a few clear differences. First of all, the wavelet analysis now exhibits only one dominant period, at $4.9t_0 = 38.1$ s, persisting for the entirety of the simulation, but with a faster decreasing signal compared to the system without thermal conduction. This dominant period is associated with the process of oscillatory reconnection, given that the secondary wavefronts generated through mode conversion are now getting dissipated faster, since anisotropic thermal conduction removes energy from the system in a very efficient way. The value for this period was calculated by finding the maximum value along the dashed lines, located at the third positive J_z peak, as shown in Figure 4. The third peak is chosen, since by then the additional the periods from the initial perturbation have decayed, while we are bordering the line with confidence level of 90%, as shown in Figure 4.

Second, the current density profile shows smaller fluctuations to its peak values. As stated before, the incoming wavefronts generated through mode conversion, which are the cause of these fluctuations, are now dissipated faster than before, due to anisotropic thermal conduction removing energy from the system in a very efficient way. If we compare the temperature profiles for the two different simulations near the X-point in Figure 5, we can see that the produced heating is not confined in small areas around the X-point any more. Instead, it is spread/conducted along the magnetic field, creating a more uniform heating profile.

As it was previously mentioned, the profiles for the current density clearly indicate that, by adding thermal conduction, the decay rate of oscillatory reconnection has increased. This is to be expected, since one of the restoring forces of the oscillation, alongside magnetic tension, is the thermal pressure force from the generated heating (McLaughlin et al. 2009). However, the heat dissipation by thermal conduction leads to a more spatially extended and uniform, as well as less prominent temperature increase, which leads to a smaller thermal pressure force and thus as weaker overall oscillation.

In order to quantify this result, we have studied the decay rate of the oscillations “envelope” for each profile. As seen in Figure 7, we have considered the local maxima of the two

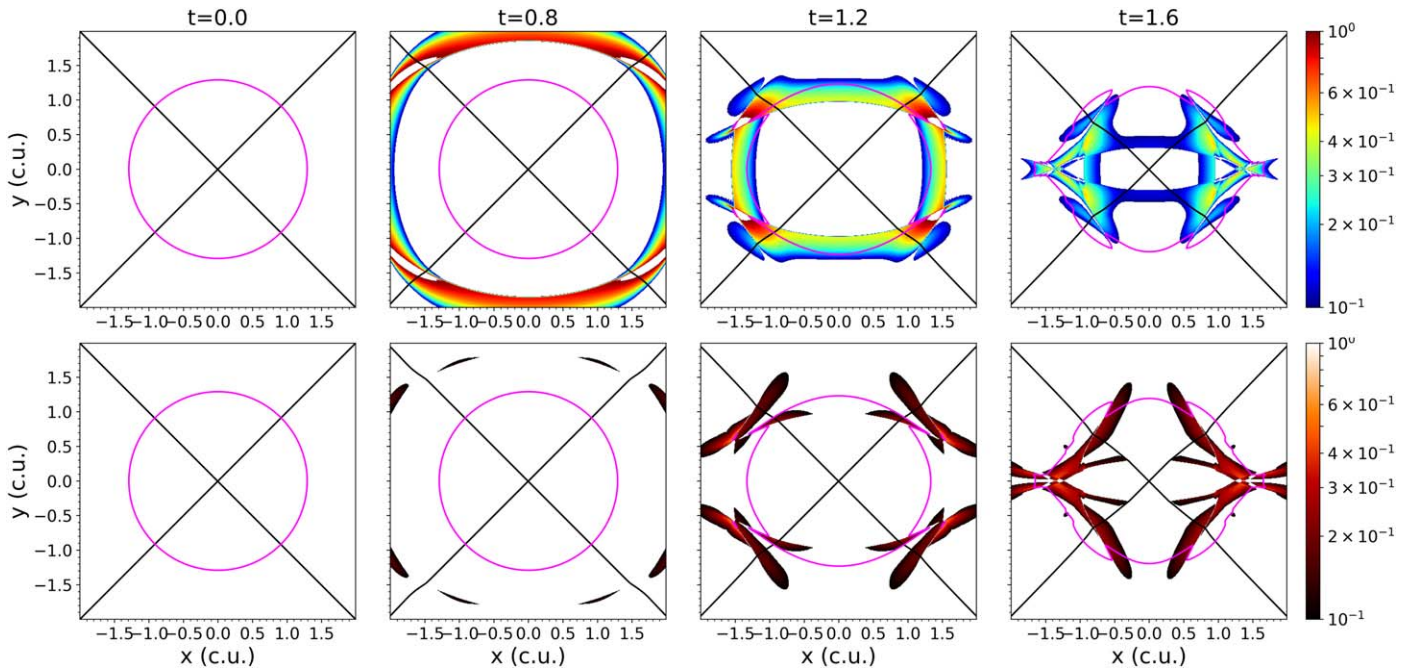


Figure 6. Zoomed in profile of the incoming pulse for the initial state of the simulation. The v_{\perp} velocity (top row) and v_{\parallel} velocity (bottom row) are shown, alongside the equipartition layer (magenta solid line) and the magnetic field separatrices (black solid lines).

oscillating profiles that can define the trend in the evolution of the oscillation amplitude. These are highlighted with red dots for the two current density profiles. By plotting the logarithm of these values as a function of time, we can divide the values in two distinct regions, as a first-order approximation. We will focus here on the first region, which is clearly associated with an exponential decay. Indeed, by fitting a linear function $f(t) = -at + b$ to the logarithmic values, we can estimate the decay rate for the two cases, $a = 0.073$ and $a = 0.124$ for the setup with and without thermal conduction, respectively. From this result, it becomes clear that, by adding thermal conduction, we end up with a faster decay for oscillatory reconnection.

3.3. The Sensitivity of Oscillatory Reconnection to Magnetic Field Strength

Studying oscillatory reconnection for hot coronal plasma and adding the effects of thermal conduction has so far provided us with very useful insight into the behavior of this mechanism in the solar corona and has put older results into perspective, as will be discussed in Section 4. However, our ultimate goal, which is beyond the scope of the current work, is to associate the mechanism of oscillatory reconnection with direct observations from the solar atmosphere and use our findings in the context of coronal seismology (e.g., Uchida 1970; Roberts et al. 1984). To that end, we want to understand the connection—if any—between the periodicity and decay rate of oscillatory reconnection at a null point, compared to the strength of the (local) magnetic field.

The first step is taken in this study, where we use our theoretical model of a magnetic field X-point configuration. We start from our basic setup, with added anisotropic thermal conduction and with a 1 MK base temperature (see Section 2.2). We will consider four cases of different equilibrium magnetic fields. One will have the “base” magnetic field ($1 \times B_0 = 1.44$ G) described in Equation (7) (note that this

is the same as that already studied in Section 3.1, albeit with a coarser resolution—see below), one with half the base magnetic field ($0.5 \times B_0 = 0.72$ G), one with double the base magnetic field ($2.0 \times B_0 = 2.88$ G), and one with triple the magnetic field strength ($3.0 \times B_0 = 4.32$ G). At the same time, we will alter the value of C in Equation (8) for the velocity pulse to ensure that we inject the same amount of kinetic energy in each setup. In particular, we will have:

1. $C = 1$, for the case with $1 \times B_0$,
2. $C = 2$, for the case with $0.5 \times B_0$,
3. $C = 1/2$, for the case with $2.0 \times B_0$, and
4. $C = 1/3$, for the case with $3.0 \times B_0$.

In this parameter study, we will use a coarser grid for our simulations (1801^2 points) in order to benefit from the faster computations. Therefore, we first need to compare with our higher resolution run (from Section 3.1) to make certain that our results are in agreement and not significantly affected by the decreased resolution. In particular, we compare the J_z current density profiles for the two resolutions, with thermal conduction present in the system. The results are shown in Figure 8. As we can see, the two profiles are in good agreement with respect to the oscillation frequency and decaying behavior. The only slight difference present is the amplitudes of the current density. In particular, they have higher absolute values for the setup with a higher resolution, since the current sheets are better resolved in that case.

The first thing to do is to study the spectra of the different J_z profiles at each null point. As seen in Figure 9, the expected oscillatory form of the profile is acquired in all the different cases, with the initial perturbation followed by the decaying oscillation. It is clear from both the profiles and the wavelet analysis that the oscillation period changes for different magnetic field strengths. In particular, starting from half the base magnetic field strength ($0.5 B_0$) and heading to higher values, the

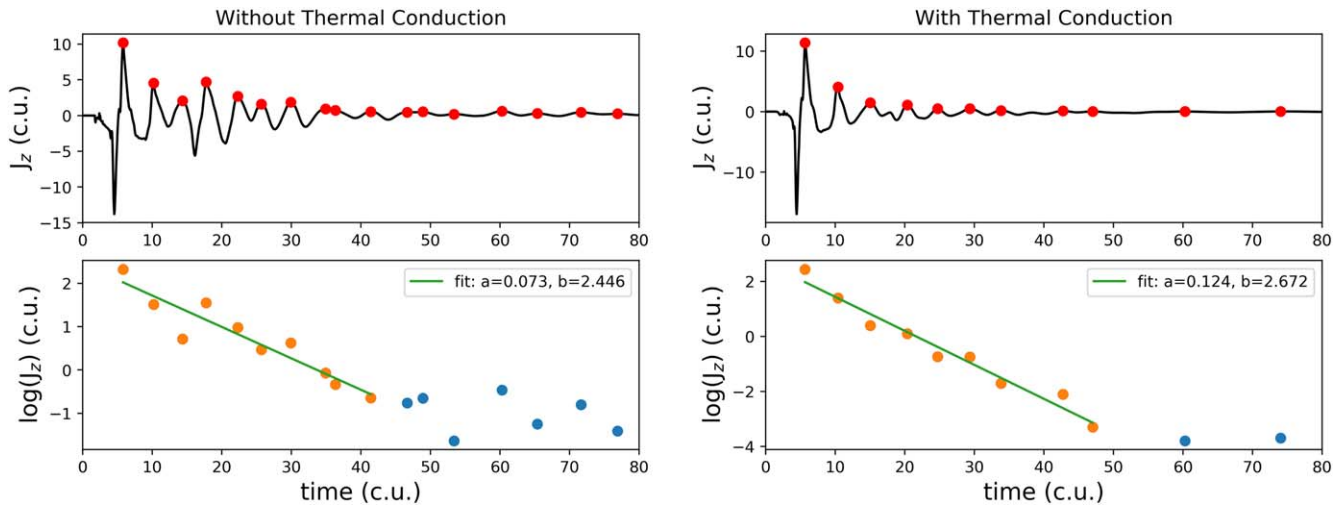


Figure 7. Top row: oscillating profile of the J_z current density at the X-point as a function of time. The red dots show the local maxima of the profile used for estimating the decay rate of the oscillation. Bottom row: logarithmic plot of the local maxima of the J_z profile. The different colored dots show the two different regions of the profile. The line fit for the decay rate is overlotted. The left panels show the results for the base setup with 1 MK, and the right panels show the results for anisotropic thermal conduction.

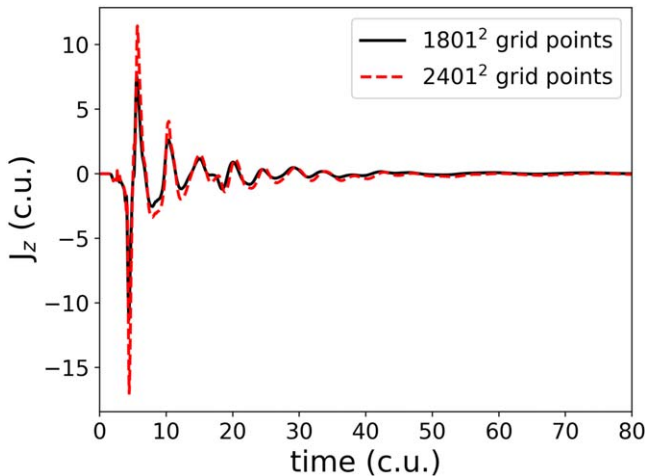


Figure 8. The J_z current density profiles at the X-point for two setups at 1 MK base temperature and anisotropic thermal conduction are overlotted. The black line corresponds to the lower-resolution setup with 1801^2 grid points, and the red dashed line to the higher resolution setup with 2401^2 grid points.

dominant period of the oscillation (as identified for the setup studied in Section 3.2) has approximate values of $6.3 t_0 = 49$ s, $4.9 t_0 = 38.1$ s, $3.1 t_0 = 24.1$ s, and finally $2.3 t_0 = 17.9$ s. For the reasons explained in the previous section, these values for the period were calculated by using a Python script to find the maximum values along the dashed lines, located at the third positive J_z peak, as shown in Figure 9. We use this method to calculate the periods for all cases, in order to be consistent. The confidence levels for these periods are above 90% with the exception of $0.5 B_0$, which shows a confidence level between 80% and 90%. Note that, for magnetic fields of $2B_0$ and $3B_0$, we only show the results up to $t = 40 t_0$, for a more convenient visualisation.

Here we need to point out that all the wavelet profiles show a peak that is associated with the initial perturbation and which has a lower period. This is usually confined in the very initial part of the oscillation and does not affect the results as time progresses. However, this peak starts to be increasingly more important for the cases with the stronger magnetic field ($2.0 \times B_0$ and

$3.0 \times B_0$), where the oscillation decays rapidly. To remain consistent with the other setups, and with the higher resolution run, we will only focus on the second peak, which is clearly associated with the decaying oscillation for those other setups.

To analyze the decay rate, we repeated the analysis with the local maxim (from Section 3.2, in order to estimate the rates of the exponential decay, as seen in Figure 10. Plots of the frequency and period versus the initial magnetic field strength can be seen in the left and middle panels of Figure 11. From the plot of the frequency, we can fit the linear function $Frequency(B_0) = c B_0 + d$, showing that the frequency is proportional to the magnetic field strength. From the plot of the period, we can fit the inverse function $Period(B_0) = 1 / Frequency(B_0)$, showing that the period seems to be inversely proportional to the magnetic field strength. This good fit for the periods and their respective frequencies is a strong indication that our calculated periods are real features of the signal and not the result of noise. For comparison, we also include a linear fit for the same plot ($Period(B_0) = c B_0 + d$, dashed line). Plotting the decay rate values for each case versus the magnetic field, we find a clear linear relation between the two, as seen in the right panel of Figure 11. Although more data points are required to confirm the exact functional relationship of this result, there is a clear trend found by this parameter study, i.e., that the period of the oscillation decreases compared to increasing magnetic field strength, and that the decay rate increases as the magnetic field strength increases.

4. Discussion and Conclusions

This paper presents an investigation of the phenomenon of oscillatory reconnection in the neighborhood of a 2D magnetic X-point for hot coronal plasma. In previous papers, this fundamental plasma mechanism has only been studied for cold plasma environments, which makes this current study an essential step for revealing more complete insight on the nature of this mechanism and its possible role in observable events in the solar atmosphere (see Section 1 for the plethora of observables that have attributed their underpinning physical mechanism to oscillatory reconnection).

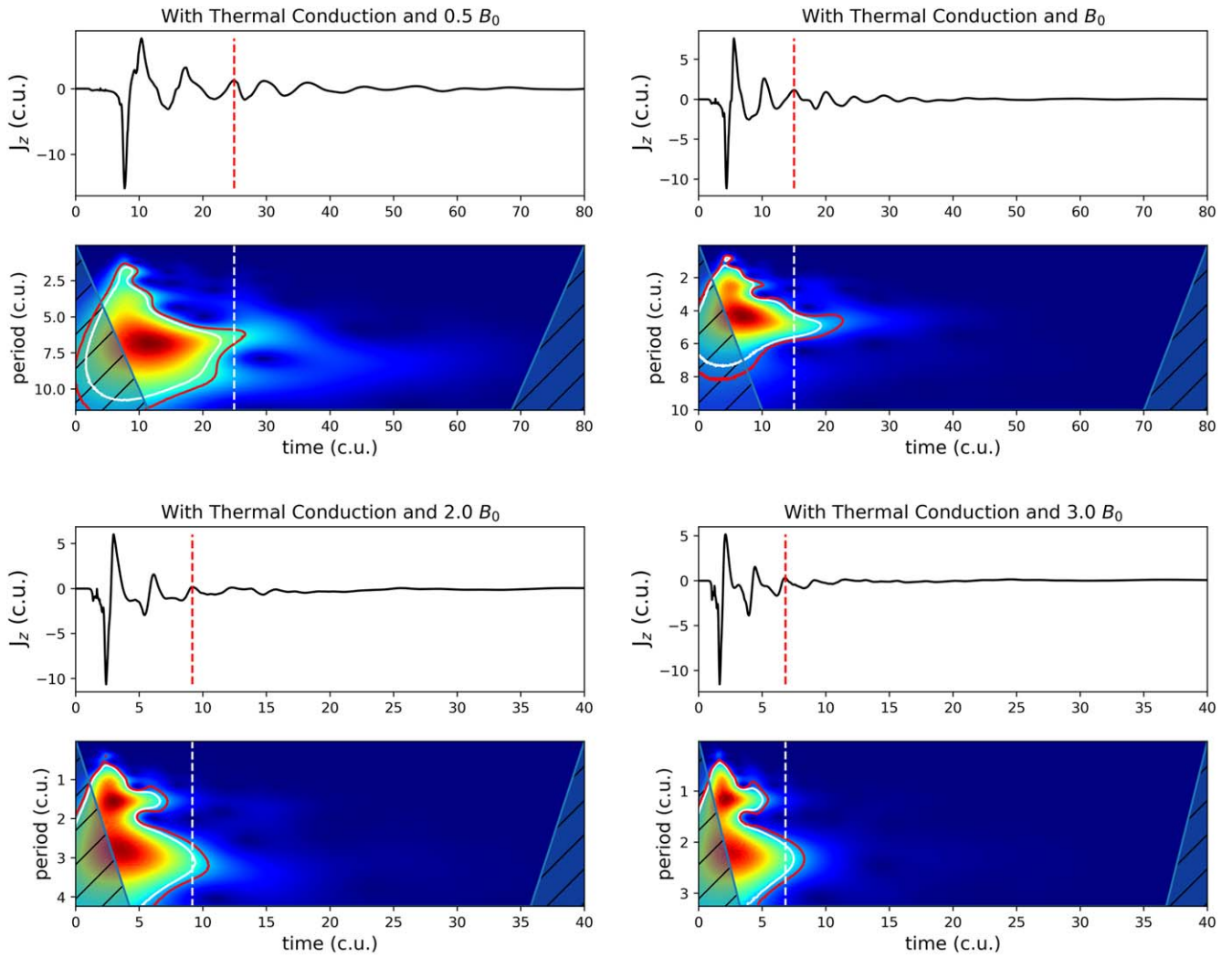


Figure 9. Same as Figure 4 but for the lower-resolution setups with anisotropic thermal conduction. The cases with different initial magnetic fields (half— $0.5 B_0$, regular - B_0 , double— $2.0 B_0$, and triple— $3.0 B_0$) are shown. Note that the profiles for double and triple the magnetic field strength show data only up to $t = 40$.

We have solved the compressible and resistive 2D MHD equations using the PLUTO code. We follow the work of McLaughlin et al. (2009) but chose to focus on hot coronal plasma instead of cold plasma. Using an initially circular velocity pulse, we initiate a fast wave that reaches the X-point, perturbing it from its equilibrium and leading to the manifestation of oscillatory reconnection. Note that all previous studies detailing the oscillatory reconnection mechanism, have utilized the LARE code (Arber et al. 2001), and so this study represents the first time that oscillatory reconnection has been studied in isolation, in the absence of other effects or instabilities, using a different code, i.e., the PLUTO code. This is important since it shows that the mechanism is not some sort of artifact associated with one particular code.

The first aspect of our study focused on oscillatory reconnection in a 1 MK hot coronal plasma. Focusing on the current density profiles at the null point, we have identified the oscillatory behavior of the process, which is connected to the periodic manifestation of horizontal and vertical current sheets. We have estimated the decay rate for the peak amplitudes of the current density, and through wavelet analysis we have revealed a complicated spectrum for the oscillating signal. The complexity of the J_z oscillating profile and spectrum is attributed to extensive mode conversion, taking place as the

v_{\perp} pulse approaches the layer where the Alfvén speed V_A equals the sound speed V_S , generating a fast and slow MHD wave in the region with high plasma- β . This phenomenon, which has already been investigated for various 2D and 3D null points (McLaughlin & Hood 2004, 2005, 2006a, 2006b; Thurgood & McLaughlin 2012), leads to an additional periodic signal superimposed on top of the oscillatory reconnection signal. This layer has a larger radius for this setup of a hot plasma, resulting in more extensive mode conversion in this case (see also the Appendix for a direct comparison of J_z profiles for setups with different equilibrium temperatures).

The second aspect of our study investigated the effect of adding anisotropic thermal conduction to our system. We found that adding anisotropic thermal conduction to our model did not prevent the development of oscillatory reconnection but led to a faster decay of the oscillation while also simplifying the spectrum of the profile. We also observed a “simpler” oscillatory profile than that of the case without thermal conduction; in particular, we report one dominant period (from the oscillatory reconnection) as opposed to two (in the absence of thermal conduction), and thus the effect of thermal conduction is twofold: it removes the significance of the generated mode-converted perturbations (since thermal conduction leads to a more effective energy dissipation from these

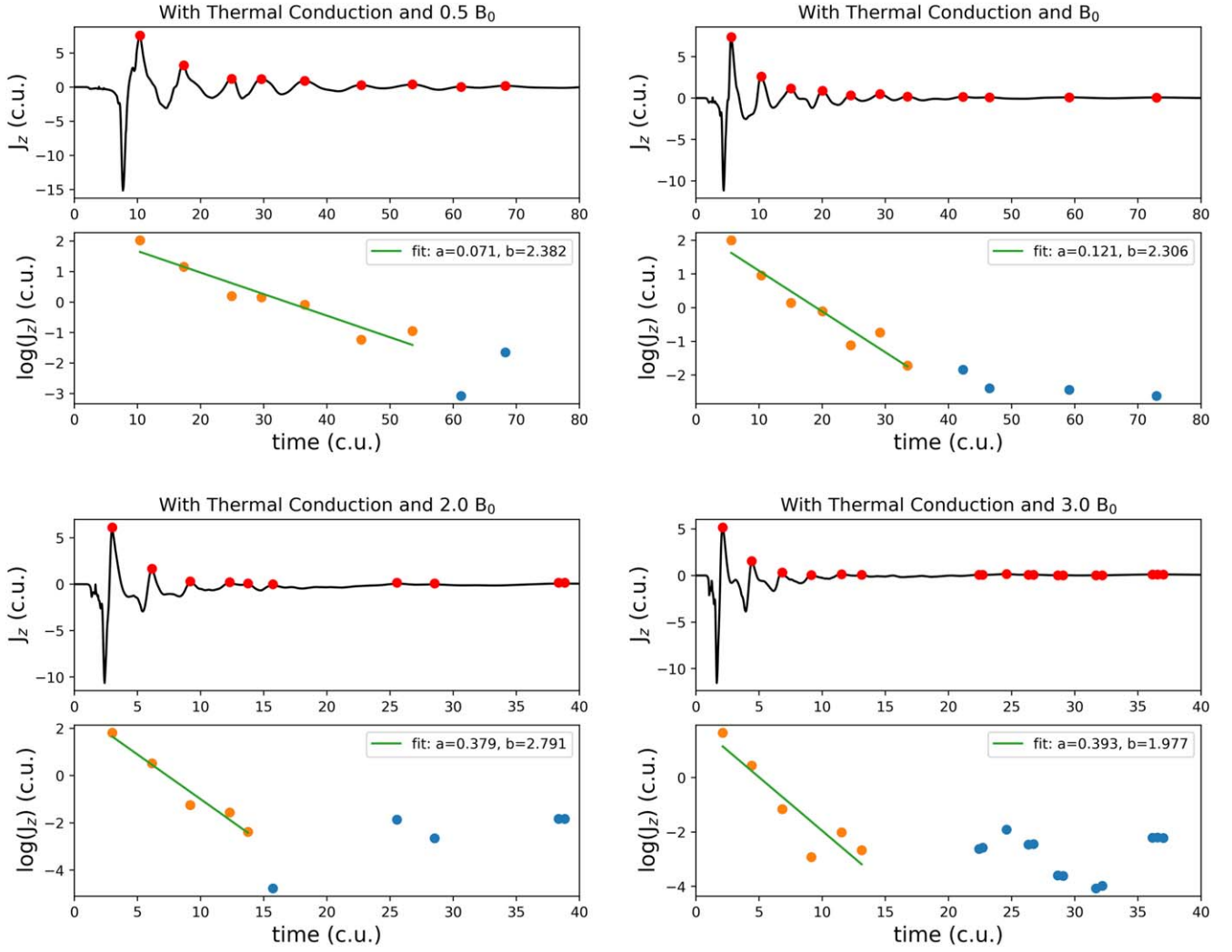


Figure 10. Same as Figure 7 but for the lower-resolution setups with anisotropic thermal conduction. The cases with different initial magnetic fields (half— $0.5 B_0$, regular - B_0 , double— $2.0 B_0$, and triple— $3.0 B_0$) are shown. Note that the profiles for double and triple the magnetic field strength show data only up to $t = 40 t_0$.

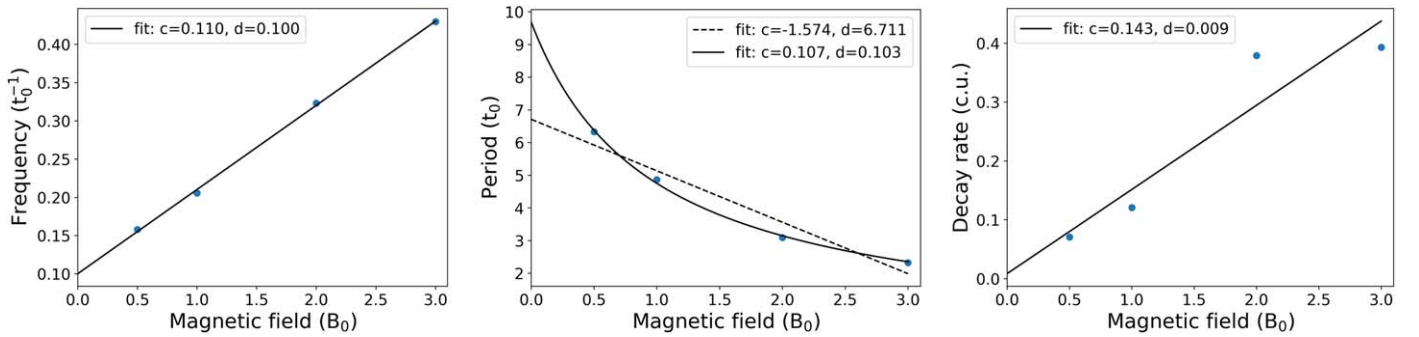


Figure 11. Left panel: frequency of the J_z oscillation profile with respect to the magnetic field strength (times the initial B_0) and a fit of the $c B_0 + d$ function. Middle panel: period of the J_z oscillation profile with respect to the magnetic field strength (times the initial B_0), and a fit of the $1/(c B_0 + d)$ (solid line) and $c B_0 + d$ (dashed line) functions. Right panel: decay rate of the J_z oscillation profile with respect to the magnetic field strength (times the initial B_0) and a fit of the linear $c B_0 + d$ function.

generated perturbations), and, second, thermal conduction leads to a faster decay of the oscillation. This second point is intuitive when considering the physical driving and restoring forces at work in oscillatory reconnection: the thermal-pressure gradients (primarily from the reconnection jets) act to sustain/

prolong the oscillation, whereas the magnetic forces act to damp the oscillation and restore the system to equilibrium. Thus, the addition of thermal conduction weakens the thermal-pressure gradients (the heat is transported away from the region of interest via the κ_{\parallel}), and consequently the system loses one of the forces

sustaining the oscillation. Thus, the system is restored to equilibrium at a faster rate, i.e., the oscillation decays at a faster rate with the addition of thermal conduction.

For the last part of this work, we performed a parameter study of hot coronal plasma with anisotropic thermal conduction present. We have found a linear relation between the magnetic field strength in the vicinity of an X-point and the decay rate of the oscillating J_z current density profile (one of the key signatures of oscillatory reconnection). This result is intuitive: magnetic forces act to restore the perturbed X-point to its equilibrium, and so stronger magnetic fields will restore the system at a faster rate, i.e., an increase in equilibrium magnetic field corresponds to an increase in decay rate. Note that, in our parameter study, we altered the initial wave amplitude to ensure we injected the same amount of kinetic energy in each setup.

We have also reported an inverse relationship between the equilibrium magnetic field and the period of oscillatory reconnection, with the respective periods ranging between 17.9 s (for a magnetic field of $3B_0 = 4.32G$) up to 49 s (for a magnetic field of $0.5B_0 = 0.72G$). In other words, stronger equilibrium magnetic fields correspond to shorter periods of oscillation (or conversely, weaker magnetic fields oscillate for longer periods). These values of the period are expected to be dependent upon the intensity of magnetic reconnection and by extension the values of the magnetic Reynolds number. Further studies are needed in order to establish a more accurate quantitative relation between the oscillation period and the magnetic field in the context of coronal plasma.

Thus, we have shown that stronger magnetic fields (relative to weaker fields) have shorter periods of oscillation as well as stronger decay rates. This demonstration opens the tantalising possibility of utilizing oscillatory reconnection as a seismological tool, and this will be the focus of future study. However, we can speculate on what aspects such a tool may want to consider: in McLaughlin et al. (2012b), it was found that the period of the oscillatory reconnection was linked to the length of the initial collapsed current sheet, i.e., the longer/stronger the first current sheet (equivalent to the first “horizontal” current sheet), the longer the resulting period.⁴ We may be seeing the same phenomena here: weaker magnetic fields form longer/stronger first current sheets and consequently have longer periods of relaxation. Conversely, strong magnetic fields form shorter first current sheets and thus have shorter periods of relaxation. Both of these results, i.e., stronger magnetic fields correspond to shorter periods of oscillation as well as stronger decay rates, can be understood by considering the “stiffness” of the magnetic field: stronger fields are more resistant to deformation and, once deformed, relax back to equilibrium at a faster rate. Again, this requires further study.

With this paper, we aim toward a better understanding of nonlinear MHD wave behavior in inhomogeneous plasma and especially in the context of the solar atmosphere. Oscillatory reconnection, in particular, is a type of fundamental time-

dependent reconnection mechanism with possible applications in several observed phenomena, including, but not limited to, QPPs (see Section 1 for several examples). To further our understanding, we need to focus on the effects of different initial conditions, such as the density distribution, temperature, and magnetic field strength of this oscillatory process. Expanding the hot plasma approach to 3D null points will provide additional insight into the wave–null point interaction. Finally, forward modeling of our results, especially for more complex magnetic field configurations, will aid us in combining these effects with the overarching aim of creating an oscillatory-reconnection-based seismological tool.

All authors acknowledge UK Science and Technology Facilities Council (STFC) support from grant ST/T000384/1. K.K. also acknowledges support by an FWO (Fonds voor Wetenschappelijk Onderzoek-Vlaanderen) postdoctoral fellowship (1273221N). This work used the Oswald High Performance Computing facility operated by Northumbria University (UK).

Appendix Equilibrium Temperature Parameter study

In the main part of the paper, we have presented our analysis on the evolution of oscillatory reconnection for a hot coronal plasma. However, in order to better understand the results, we need a more direct comparison with the cold plasma case. To that end, we present here a parameter study that will investigate the differences of oscillatory reconnection for different initial equilibrium temperatures. We will consider a basic setup similar to the one described in Section 2. For this study, we will use ideal MHD in the presence of numerical resistivity, without the use of anisotropic thermal conduction. We will be using the same Runge–Kutta method for the time step, the same solver (TVDLF), and the Constrained Transport method for keeping the solenoidal constraint. Since this is a parameter study and we want to benefit from faster computations, we use a resolution of 1801^2 grid points.

Another difference from the (higher-resolution) base setup that we have focused on, is the use of different spatial integration schemes. For all the other cases previously considered, we had included the fifth-order monotonicity preserving scheme (MP5) for the spatial integration, which provides the highest-accuracy results for a given resolution from all the methods provided with the PLUTO code. However, this scheme is unstable for simulations with cold plasma, in the context of the current setup. Therefore, for this parameter study, we have used a slightly more stable, and currently the second most accurate method provided by the PLUTO code: the parabolic reconstruction method.

Our first step is to compare the results from the two different reconstruction methods for a known solution. In the left panel of Figure 12, we take the high-resolution run without thermal conduction, which was studied in Section 3.1, and we compare it with its equivalent setup at the decreased resolution. Then both of these are compared to the decreased resolution setup with the parabolic reconstruction method. From Figure 12, we can see that comparison of the two profiles for the MP5 method are very similar in frequency and overall behavior. In fact, just like in Figure 8, the only difference between the two (red dashed line and black solid line) are the amplitudes of the J_z current density. When we then compare the two lower-resolution runs (black solid line and orange solid line), we

⁴ Note that McLaughlin et al. (2012b) also found a positive relationship between the magnetic field strength of a subphotospheric, initially buoyant flux tube and the resultant period, and thus at first sight this result appears to disagree with our findings here. However, McLaughlin et al. (2012b) found that the stronger the magnetic field strength of the emerging flux tube, the longer the initial current sheet formed (i.e., formed when the flux emerged into a preexisting magnetic environment) and those longer initial current sheets corresponded to longer periods. In other words, McLaughlin et al. (2012b) found that it is the length of the initial current sheet that is important to understand resultant periods (and that, in their system, stronger flux emergence corresponded to generating longer initial current sheets).

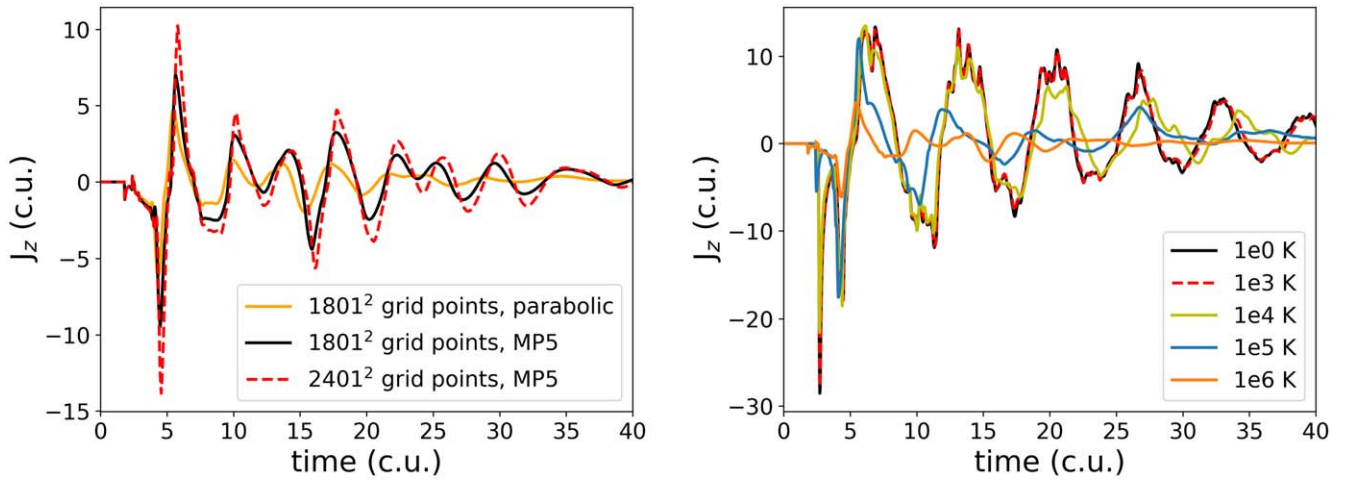


Figure 12. Left panel: a comparison plot of different setups with 1 MK base temperature without thermal conduction. Two of the profiles are for the lower-resolution setups but for different spatial reconstruction methods (MP5 and Parabolic), and the third is for the high resolution setup with the MP5 spatial reconstruction method. This plot connects the results of the temperature parameter study to the high-resolution base setup on which we focused in this study. Right panel: plot of the J_z current density profile for all the setups with the different base temperatures that were used in this parameter study. For these setups, we have not used thermal conduction.

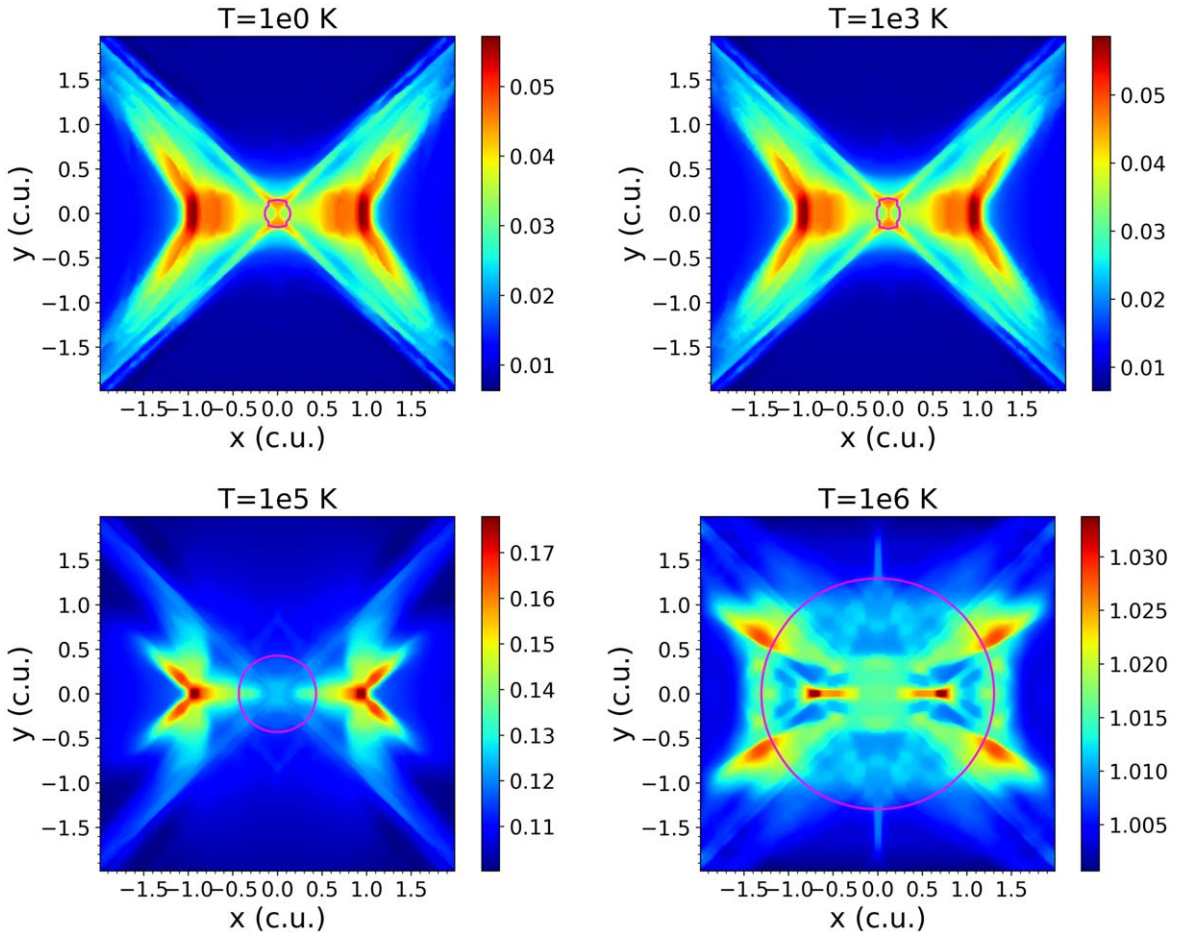


Figure 13. Temperature profiles for four setups with different initial base temperatures (at 1 K, 10^4 K, 10^5 K, and 10^6 K). The profiles are showing snapshots at $t = 40$, in code units. The equipartition layer for each profile is also plotted. Note that the color scale is different for each profile.

again see a similar oscillatory behavior and periodicity. The MP5 method yields stronger values for the peaks of the current density at the same resolution, which also better resolves the oscillation at the later part of the simulation. However, the accuracy of the parabolic reconstruction is adequate in order to employ it for the parameter study.

In the right panel of Figure 12, we see a combined plot of the J_z profiles of all the cases. We consider setups with base temperatures of 1, 10^3 , 10^4 , 10^5 , and 10^6 K. In all these cases, the same magnetic field, density, and initial velocity pulse are considered. The first obvious result is that, in all cases, we have oscillatory reconnection manifesting. Each setup exhibits a

different initial perturbation amplitude, for the same initial condition from Equations (8) and (9), with the hotter setups showing smaller overall amplitudes and relatively smaller oscillation periods. This seems counterintuitive, since in Thurgood et al. (2019) it was found that, for the nonlinear regime, stronger initial perturbations would lead to smaller oscillation periods. However, that study did not take into account differences that may occur from varying initial conditions, as in the temperature in our cases.

We also see that the lower temperature runs (with 1 and 10^3 K) exhibit an almost identical evolution for the oscillation of the current density profiles. To understand why, one needs to see the temperature profile panels of Figure 13. These profiles show the temperature near the X-point at time $t = 40t_0$. Due to the very low base temperature of the first two profiles (1 and 10^3 K), the heating from the oscillatory reconnection heats up the plasma near the null point to practically the same temperature. In fact, the only notable difference between the two profiles shown here is the shape of the equipartition layer.

Once we start increasing the base temperature of our setup, for the same base magnetic field, we start seeing some of the aforementioned additional, superimposed periodic signals in the oscillatory profiles. As we have explained (Section 3.1), these additional periodic signals can be attributed to the more extensive mode conversion taking place near the equipartition layer and inside the area that is included. Indeed, the more prominent additional periodic signals are seen for the two hotter setups, which also show the equipartition layers with the largest radii. Thus, we can now compare the results of our main study with those for cold plasma and obtain a better understanding of our previous findings.

ORCID iDs

Konstantinos Karampelas  <https://orcid.org/0000-0001-5507-1891>
 James A. McLaughlin  <https://orcid.org/0000-0002-7863-624X>
 Gert J. J. Botha  <https://orcid.org/0000-0002-5915-697X>
 Stéphane Régnier  <https://orcid.org/0000-0001-8954-4183>

References

- Arber, T. D., Longbottom, A. W., Gerrard, C. L., & Milne, A. M. 2001, *JCoPh*, **171**, 151
- Bale, S. D., Badman, S. T., Bonnell, J. W., et al. 2019, *Natur*, **576**, 237
- Bale, S. D., Goetz, K., Harvey, P. R., et al. 2016, *SSRv*, **204**, 49
- Broomhall, A. M., Thomas, A. E. L., Pugh, C. E., Pye, J. P., & Rosen, S. R. 2019, *A&A*, **629**, A147
- Brown, D. S., & Priest, E. R. 2001, *A&A*, **367**, 339
- Cattell, C., Glesener, L., Leiran, B., et al. 2021, *A&A*, **650**, A6
- Clarke, B. P., Hayes, L. A., Gallagher, P. T., Maloney, S. A., & Carley, E. P. 2021, *ApJ*, **910**, 123
- Craig, I. J. D., & McClymont, A. N. 1991, *ApJL*, **371**, L41
- Cranmer, S. R. 2018, *ApJ*, **862**, 6
- De Pontieu, B., & McIntosh, S. W. 2010, *ApJ*, **722**, 1013
- De Pontieu, B., McIntosh, S. W., Carlsson, M., et al. 2007, *Sci*, **318**, 1574
- De Pontieu, B., McIntosh, S. W., Carlsson, M., et al. 2011, *Sci*, **331**, 55
- Galsgaard, K., & Nordlund, Å. 1997, *JGR*, **102**, 231
- Gibson, S., Kucera, T., White, S., et al. 2016, *FrASS*, **3**, 8
- Gruszecki, M., Vasheghani Farahani, S., Nakariakov, V. M., & Arber, T. D. 2011, *A&A*, **531**, A63
- Guarcello, M. G., Micela, G., Sciortino, S., et al. 2019, *A&A*, **622**, A210
- Hayes, L. A., Inglis, A. R., Christe, S., Dennis, B., & Gallagher, P. T. 2020, *ApJ*, **895**, 50
- He, J., Marsch, E., Tu, C., & Tian, H. 2009, *ApJL*, **705**, L217
- He, J., Zhu, X., Yang, L., et al. 2021, *ApJL*, **913**, L14
- Heyvaerts, J., & Priest, E. R. 1983, *A&A*, **117**, 220
- Hong, J., Yang, J., Chen, H., et al. 2019, *ApJ*, **874**, 146
- Jackman, J. A. G., Wheatley, P. J., Pugh, C. E., et al. 2019, *MNRAS*, **482**, 5553
- Karpen, J. T., DeVore, C. R., Antiochos, S. K., & Pariat, E. 2017, *ApJ*, **834**, 62
- Kasper, J. C., Bale, S. D., Belcher, J. W., et al. 2019, *Natur*, **576**, 228
- Kupriyanova, E., Kolotkov, D., Nakariakov, V., & Kaufman, A. 2020, *STP*, **6**, 3
- Kupriyanova, E. G., Kashapova, L. K., Reid, H. A. S., & Myagkova, I. N. 2016, *SoPh*, **291**, 3427
- Li, D., Feng, S., Su, W., & Huang, Y. 2020a, *A&A*, **639**, L5
- Li, D., Ge, M., Dominique, M., et al. 2021, *ApJ*, **921**, 179
- Li, D., Lu, L., Ning, Z., et al. 2020b, *ApJ*, **893**, 7
- Lin, H., Kuhn, J. R., & Coulter, R. 2004, *ApJL*, **613**, L177
- Longcope, D. W. 2005, *LRSP*, **2**, 7
- Lynch, B. J., Edmondson, J. K., & Li, Y. 2014, *SoPh*, **289**, 3043
- Mancuso, S., Barghini, D., & Telloni, D. 2020, *A&A*, **636**, A96
- McIntosh, S. W., de Pontieu, B., Carlsson, M., et al. 2011, *Natur*, **475**, 477
- McLaughlin, J. A., De Moortel, I., Hood, A. W., & Brady, C. S. 2009, *A&A*, **493**, 227
- McLaughlin, J. A., & Hood, A. W. 2004, *A&A*, **420**, 1129
- McLaughlin, J. A., & Hood, A. W. 2005, *A&A*, **435**, 313
- McLaughlin, J. A., & Hood, A. W. 2006a, *A&A*, **452**, 603
- McLaughlin, J. A., & Hood, A. W. 2006b, *A&A*, **459**, 641
- McLaughlin, J. A., Hood, A. W., & de Moortel, I. 2011, *SSRv*, **158**, 205
- McLaughlin, J. A., Nakariakov, V. M., Dominique, M., Jelínek, P., & Takasao, S. 2018, *SSRv*, **214**, 45
- McLaughlin, J. A., Thurgood, J. O., & MacTaggart, D. 2012a, *A&A*, **548**, A98
- McLaughlin, J. A., Verth, G., Fedun, V., & Erdélyi, R. 2012b, *ApJ*, **749**, 30
- Mignone, A., Bodo, G., Massaglia, S., et al. 2007, *ApJS*, **170**, 228
- Mignone, A., Zanni, C., Tzeferacos, P., et al. 2012, *ApJS*, **198**, 7
- Murray, M. J., van Driel-Gesztelyi, L., & Baker, D. 2009, *A&A*, **494**, 329
- Nakariakov, V. M., Foullon, C., Verwichte, E., & Young, N. P. 2006, *A&A*, **452**, 343
- Nakariakov, V. M., & Verwichte, E. 2005, *LRSP*, **2**, 3
- Nishizuka, N., Shimizu, M., Nakamura, T., et al. 2008, *ApJL*, **683**, L83
- Notsu, Y., Maehara, H., Honda, S., et al. 2019, *ApJ*, **876**, 58
- Okamoto, T. J., Tsuneta, S., Berger, T. E., et al. 2007, *Sci*, **318**, 1577
- Orlando, S., Bocchino, F., Reale, F., Peres, G., & Pagano, P. 2008, *ApJ*, **678**, 274
- Parker, E. N. 1957, *JGR*, **62**, 509
- Petschek, H. E. 1964, in *The Physics of Solar Flares*, Proc. AAS-NASA Symp., ed. W. N. Hess, 50 (Washington, DC: NASA), 425
- Priest, E., & Forbes, T. 2000, *Magnetic Reconnection* (Cambridge: Cambridge Univ. Press)
- Pugh, C. E., Nakariakov, V. M., Broomhall, A. M., Bogomolov, A. V., & Myagkova, I. N. 2017, *A&A*, **608**, A101
- Ramsay, G., Kolotkov, D., Doyle, J. G., & Doyle, L. 2021, *SoPh*, **296**, 162
- Régnier, S., Parnell, C. E., & Haynes, A. L. 2008, *A&A*, **484**, L47
- Roberts, B., Edwin, P. M., & Benz, A. O. 1984, *ApJ*, **279**, 857
- Sabri, S., Ebadi, H., & Poedts, S. 2020, *ApJ*, **902**, 11
- Sabri, S., Poedts, S., & Ebadi, H. 2019, *A&A*, **623**, A81
- Sabri, S., Vasheghani Farahani, S., Ebadi, H., Hosseinpour, M., & Fazel, Z. 2018, *MNRAS*, **479**, 4991
- Samanta, T., Tian, H., Yurchyshyn, V., et al. 2019, *Sci*, **366**, 890
- Santamaria, I. C., Khomenko, E., & Collados, M. 2015, *A&A*, **577**, A70
- Santamaria, I. C., Khomenko, E., Collados, M., & de Vicente, A. 2016, *A&A*, **590**, L3
- Santamaria, I. C., Khomenko, E., Collados, M., & de Vicente, A. 2017, *A&A*, **602**, A43
- Santamaria, I. C., & Van Doorselaere, T. 2018, *A&A*, **611**, A10
- Shen, Y., Liu, Y., Song, T., & Tian, Z. 2018, *ApJ*, **853**, 1
- Shibata, K., & Magara, T. 2011, *LRSP*, **8**, 6
- Sweet, P. A. 1958, in *IAU Symp. 6, Electromagnetic Phenomena in Cosmical Physics*, ed. B. Lehnert (Cambridge: Cambridge Univ. Press), 123
- Thurgood, J. O., & McLaughlin, J. A. 2012, *A&A*, **545**, A9
- Thurgood, J. O., & McLaughlin, J. A. 2013, *A&A*, **558**, A127
- Thurgood, J. O., Pontin, D. I., & McLaughlin, J. A. 2017, *ApJ*, **844**, 2
- Thurgood, J. O., Pontin, D. I., & McLaughlin, J. A. 2018a, *ApJ*, **855**, 50
- Thurgood, J. O., Pontin, D. I., & McLaughlin, J. A. 2018b, *PhPl*, **25**, 072105
- Thurgood, J. O., Pontin, D. I., & McLaughlin, J. A. 2019, *A&A*, **621**, A106
- Tomczyk, S., McIntosh, S. W., Keil, S. L., et al. 2007, *Sci*, **317**, 1192
- Uchida, Y. 1970, *PASJ*, **22**, 341
- Van Doorselaere, T., Kupriyanova, E. G., & Yuan, D. 2016, *SoPh*, **291**, 3143
- Vida, K., Oláh, K., Kóvári, Z., et al. 2019, *ApJ*, **884**, 160
- Xue, Z., Yan, X., Jin, C., et al. 2019, *ApJL*, **874**, L27
- Yuan, D., Feng, S., Li, D., Ning, Z., & Tan, B. 2019, *ApJL*, **886**, L25
- Yurchyshyn, V., Cao, W., Abramenko, V., Yang, X., & Cho, K.-S. 2020, *ApJL*, **891**, L21
- Zimovets, I. V., McLaughlin, J. A., Srivastava, A. K., et al. 2021, *SSRv*, **217**, 66